

Category-Level Pose Retrieval with Contrastive Features Learnt with Occlusion Augmentation

Georgios Kouros¹
georgios.kouros@esat.kuleuven.be

Shubham Shrivastava²
sshri5@ford.com

Cédric Picron¹
cedric.picron@esat.kuleuven.be

Sushruth Nagesh²
snagesh1@ford.com

Punarjay Chakravarty²
pchakra5@ford.com

Tinne Tuytelaars¹
tinne.tuytelaars@esat.kuleuven.be

¹ PSI, ESAT
KU Leuven
Belgium

² Ford Greenfield Labs
Palo Alto, USA

Abstract

Pose estimation is usually tackled as either a bin classification problem or as a regression problem. In both cases, the idea is to directly predict the pose of an object. This is a non-trivial task because of appearance variations of similar poses and similarities between different poses. Instead, we follow the key idea that it is easier to compare two poses than to estimate them. Render-and-compare approaches have been employed to that end, however, they tend to be unstable, computationally expensive, and slow for real-time applications. We propose doing category-level pose estimation by learning an alignment metric using a contrastive loss with a dynamic margin and a continuous pose-label space. For efficient inference, we use a simple real-time image retrieval scheme with a reference set of renderings projected to an embedding space. To achieve robustness to real-world conditions, we employ synthetic occlusions, bounding box perturbations, and appearance augmentations. Our approach achieves state-of-the-art performance on PASCAL3D and OccludedPASCAL3D, as well as high-quality results on KITTI3D.

1 Introduction

Estimating the pose of a 3D rigid object is a fundamental task in numerous computer vision applications. For instance, a self-driving vehicle must be able to estimate the pose of other road users in its surroundings in order to navigate safely without endangering itself or others. Deep learning has revolutionized such pose estimation tasks especially for challenging

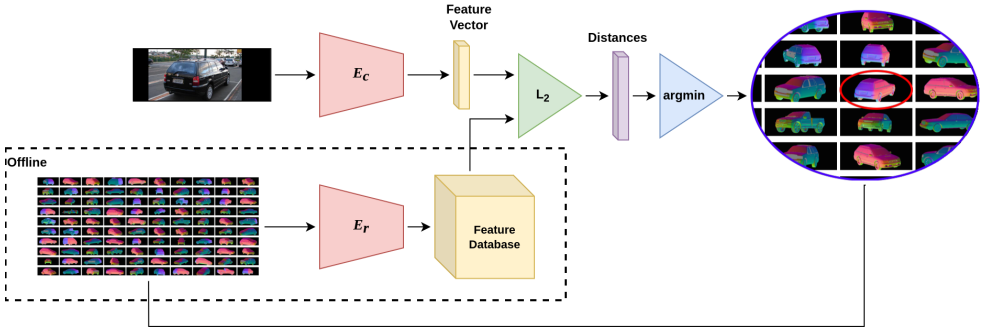


Figure 1: Using a properly learned metric, all it takes to estimate the pose of an object with state-of-the-art accuracy is a simple retrieval scheme that finds the most similar rendered image in a database.

monocular settings [11, 12, 13, 14, 15, 16, 17] compared to stereo [18, 19, 20, 21, 22] or RGB-D [23, 24] settings that leverage 3D information from their inputs. Two ongoing problems are how to best extract 3D information from 2D image inputs and how to achieve real-time operation and robustness even in complex and cluttered real-world scenes.

Previous methods approach pose estimation as either a classification [25], regression [26, 27, 28, 29] or optimization problem [30, 31, 32]. Classification and regression have to directly predict the pose as either belonging to a bin or as a set of continuous values. On the other hand, optimization methods such as render-and-compare approaches iteratively optimize the pose. Comparing two images with regard to their pose can be considered a much easier task to learn. Nevertheless, such an iterative optimization approach, although accurate, may be too slow for real-time category-level pose estimation.

In this work, we propose a multimodal contrastive learning framework for extracting discriminative features from real-world images and renderings that can be used for comparing the two images with regard to their poses. Rather than following a slow iterative approach similar to render-and-compare methods [33, 34], we propose to compare the feature embedding of a query image with a reference set of embeddings from rendered objects in various poses. We also increase robustness to complex and cluttered scenes by augmenting training images with appearance variations, bounding box perturbations, and synthetic occlusions. Our main contributions can be summarized as follows:

- We propose a simple yet effective category-level pose retrieval framework based on learning discriminative features using contrastive learning with a dynamic margin.
- We show that strong data augmentation can enhance a simple pose estimation architecture to outperform more complex ones.
- We report state-of-the-art results on PASCAL3D and OccludedPASCAL3D, as well as high quality cross-dataset performance on KITTI3D.

2 Related Work

Monocular pose estimation can be described as an ill-posed problem due to the lack of 3D information, although, good empirical results have been obtained. Recovering 3D informa-

tion is usually accomplished through either monocular depth prediction [0, 12, 13] or by incorporating prior hypotheses about the objects such as shape priors for template matching [0, 14, 15, 16] in render-and-compare or image retrieval settings. In this work, we utilize prior shape hypotheses in the form of CAD models for category-level pose estimation. We specifically target category-level methods to achieve a good trade-off between accuracy, generalization, and robustness to occlusions and clutter compared to instance-based and category-agnostic methods.

In the scope of render-and-compare approaches, RePose [14] runs faster than real-time by optimizing the pose of an object with learned deep textures, but is applicable only at the instance-level. Beker *et al.* [0] and Wang *et al.* [16] propose render-and-compare methods for estimating the pose and shape of cars using photometric, depth, or silhouette comparison, but without achieving real-time performance. NeMo [15], on the other hand, uses a generative neural mesh model and contrastive learning to first learn discriminative features that distinguish objects from occlusions and background clutter before optimizing the pose through render-and-compare for approximately 8 seconds per object. To avoid the overhead of render-and-compare optimization, we choose a simple yet efficient image retrieval setting.

Retrieval-based methods rely on a good comparison metric and deep metric learning with contrastive [6] or triplet-like [28] losses has been instrumental towards that end. Wohlhart and Lepetit [19] first proposed to use a triplet-like loss to optimize a CNN feature extractor for instance-level pose estimation tasks based on nearest neighbour retrieval. Zhakarov *et al.* [10] augmented the triplet-like loss with a dynamic margin that considers both the object instance and the pose distance between anchor/positive and negative samples. All aforementioned methods, however, discretize the pose space into bins with a negative impact on accuracy. Papaioannidis and Pitas [24] added a regression loss term that both improved performance and enabled direct pose regression instead of slow nearest neighbour search. PoseContrast [18] is trained with a loss function, combining classification, regression, and contrastive loss terms, on real data with pose-aware augmentations and without prior geometry knowledge. In this work, we propose a simple contrastive loss with a dynamic margin and a continuous pose space achieved by choosing positive and negative pairs and optimizing according to pose distance rather than binning. In our case, each pair consists of a real image (anchor) and a rendering of a CAD model (positive/negative), for which we jointly train two individual feature extractor CNNs.

Achieving robustness to foreground occlusions and background clutter usually requires complex architectures and loss functions. For instance, NeMo [15] employs contrastive learning to learn to distinguish between object features and background clutter or foreground occlusions. A different approach [10] suggests simply augmenting input images with synthetic occlusions to increase robustness in human pose estimation tasks. On a similar note, we adopted this occlusion augmentation in the pose estimation of 3D rigid objects.

3 Method

3.1 Learning Discriminative Pose Features

The main idea in deep metric learning is to optimize a high-dimensional embedding feature space (manifold) so that samples are pulled together or pushed apart depending on whether they belong to the same class or not. For example, such an embedding space can be optimized

using the Contrastive Loss [5] defined as

$$\mathcal{L} = \frac{1}{2N} \sum_{i=1}^N \left[(1 - y_i) \|f_{1,i} - f_{2,i}\|_2^2 + y_i \max(0, m - \|f_{1,i} - f_{2,i}\|_2^2) \right], \quad (1)$$

where N is the batch size, m is the margin, f_1, f_2 are the embedding/encoder functions, and y_i is a label that is 1 if the pair is positive and 0 if negative.

Applying deep metric learning for pose estimation would thus require discretizing the pose space and assigning the pose labels to bins as in [35, 40]. However, this means that slightly different poses might fall in different bins and thus the network would be encouraged to separate them in feature space, which would negatively impact generalization to unseen poses. Consequently, similar to the Triplet-like Dynamic Margin Loss [40], we employ a dynamic margin that is proportional to the pose distance between two samples. In contrast to [40], we train our models for pose estimation on the category-level rather than the instance-level, and avoid the discretization of the pose-label space that negatively impacts accuracy. While they use the discretized pose labels to determine positive and negative sample pairs, we propose a continuous pose-label space and determine positive and negative pairs by applying a threshold on the pose distance. As a result, we redefine the Contrastive Loss from Equation 1 to our *Contrastive Pose Loss* expressed as

$$\mathcal{L} = \frac{1}{2N} \sum_{i=1}^N \left[(1 - y_i) \max(0, \|f_{1,i} - f_{2,i}\|_2^2 - m\Delta\theta) + y_i \max(0, m\Delta\theta - \|f_{1,i} - f_{2,i}\|_2^2) \right], \quad (2)$$

where $\Delta\theta = 2 \cos^{-1}(|q_i \cdot q_j|)$ denotes the geodesic distance between two quaternions q_i, q_j .

3.2 Sampling and Mining

According to numerous works [10, 13, 22, 26, 28, 34, 40], Deep Metric Learning performance is heavily influenced by the selection of samples in a mini-batch during training and thus a sophisticated scheme is essential to speeding up convergence.

Datasets often suffer from imbalance, such as typical car datasets having more sedan cars than vans, which may result in poorer performance in the latter subcategory. This can be alleviated by a sampling scheme that weights each sample inversely proportional to the number of occurrences of its subcategory, an idea inspired by the Focal Loss [20]. In addition, for every sample already chosen for a batch, the sampling scheme aims to include $N \geq 1$ additional samples with a similar pose (e.g. less than 5° difference) because they are more likely to have a small feature distance that needs to be optimized.

We also designed a pose-aware miner that looks for pairs of samples violating the pose margin, resulting in higher losses and thus more efficient optimization. The sampler feeds the miner a mini-batch of N indices corresponding to N samples composed of a camera image and its rendered counterpart. All possible positive and negative pairs are constructed based on a threshold (e.g. 5°), of which all pairs that violate the pose margin are used to calculate the loss. The rest are dropped since they do not offer any value to the optimization.

3.3 Rendering

In contrast to NeMo [10] and similar to [40], we do not use a 3D generative model for producing the renderings, but rather employ a more conventional approach of generating 2D

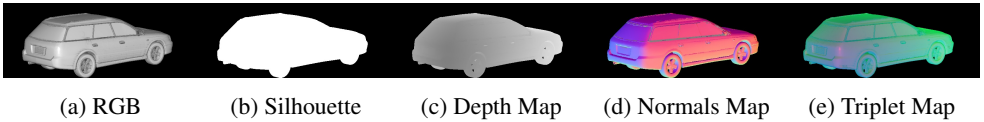


Figure 2: Five types of renderings that were evaluated for pose estimation.



Figure 3: Examples of synthetic occlusions for various scale factors

mesh renderings, silhouettes, surface normal maps, depth maps, or even multi-channel RGB-depth-normal combinations that were inspired from [9], and which we call triplets. It is our intuition that using such feature representations, as illustrated in Figure 2, preserves perspective information vital to pose estimation tasks as opposed to the 3D generative model used by NeMo. Rather than generating a set of renderings for the entire viewing sphere, we create a rendering database by generating one rendering per sample in the training set thus ensuring at least one positive per sample. This approach requires less space and less time for inference while avoiding the need to find a trade-off between discretization error and size of the database. Moreover, this naturally reflects the prior distribution over the viewing sphere.

3.4 Robustness to Occlusions

To increase robustness to occlusions and background clutter, we use data augmentation with synthetic occlusions [50] produced from PASCAL VOC 2012 [6]. This involves segmenting objects from PASCAL VOC to create a template set of occluders from 20 object categories. An input image is then augmented with one to eight randomly selected occluders which are visually, spatially, and geometrically augmented. When training with a specific object class we naturally filter out that class from the occluder set to avoid having objects from that class occluding the actual object of interest. Finally, for tuning purposes we use a tunable occlusion scale s_{occ} and a random resize factor $x \sim U[0, 1]$ to resize an occluder

$$f_x = f_y = s_{occ} x, \quad (3)$$

where f_x and f_y are the resizing factors for the horizontal and vertical dimensions, respectively. Figure 3 illustrates occlusion augmentations and the effect of s_{occ} .

3.5 Robustness to Bounding Box Noise

Throughout the experiments we assume known scale and center of the objects similar to NeMo [4]. Practically, this is not realistic and although NeMo implies some basic tolerance to center/scale perturbations, it is designed in such a way that works optimally with aligned center and scale between camera image and renderings. In order to avoid this restriction we propose augmenting training samples with random bounding box noise with a lower boundary on IoU. To define this type of noise we express the deviation of the bounding box corners as a function of the lower IoU boundary. If w and h are the width and height of the

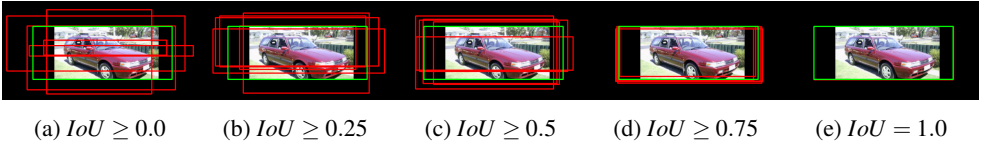


Figure 4: Artificial bounding box noise with a lower boundary on IoU. Green denotes the original image borders and red denotes randomly perturbed bounding boxes.

bounding box and n the maximum horizontal and vertical corner deviation in pixels, then

$$IoU_{min} = \frac{(w - 2n)(h - 2n)}{wh}. \quad (4)$$

By solving the quadratic equation we can calculate the maximum pixel deviation n as a function of IoU_{min} via the equation

$$n = \frac{h + w - \sqrt{(h + w)^2 - 4wh\beta}}{4}, \quad (5)$$

where $\beta = 1 - IoU_{min}$ is the noise scale parameter used in the experiments. Figure 4 presents a few examples of our bounding box noise scheme for different IoU lower boundaries.

3.6 Inference via Pose Retrieval

After jointly training the camera and rendering encoders E_c and E_r , corresponding to encoding functions f_1 and f_2 from equation 2, we can predict poses through a simple image retrieval scheme, as shown in Figure 1. Our inference framework requires an offline step of generating a reference set of renderings which need to be embedded using encoder E_r and stored for online inference. Inferring the pose is then basically a two-step-approach composed of encoding a query image with encoder E_c , calculating the L_2 distance of the query embedding to all feature embeddings in the stored reference set, and finally finding the nearest neighbour, whose label corresponds with our predicted pose.

4 Experiments

4.1 Experimental Setup

Our framework was developed using *PyTorch* [43], *PyTorch Metric Learning* [44], and *PyTorch3D* [45]. We jointly train two ResNet50 [46] encoders E_c and E_r as shown in Figure 1. MLP heads are used to further reduce the dimensionality of the feature space from 2048 to 512. Each model was trained on an NVidia Titan V GPU with 12GB of memory for approximately 2-3 days. For evaluation, we used the test set images as the query set and the training renderings as the reference set.

We trained with a batch size of 32 for 1000 epochs using the Adam Optimizer [47] with a learning rate of $= 10^{-4}$ for the ResNet50 encoders and 10^{-3} for the MLP heads and with a weight decay of $5 \cdot 10^{-4}$. The embedding size was set to 512 and the loss margin was set to $m = 1.0$. For sampling and mining we used a positive/negative threshold $t_{\Delta\theta} = 5^\circ$. Finally, unless stated otherwise, we use $\beta_{train} = 0.1$ and $s_{occ} = 0.5$. To make a more fair evaluation,

	Categ. aware	$ACC_{\frac{\pi}{6}} \uparrow$				$ACC_{\frac{\pi}{18}} \uparrow$				$MedErr \downarrow$			
		L0	L1	L2	L3	L0	L1	L2	L3	L0	L1	L2	L3
Res50-A [†]		88.1	70.4	52.8	37.8	44.6	25.3	14.5	6.7	11.7	17.9	30.4	46.4
Res50-S [†]	✓	87.6	73.2	58.4	43.1	43.9	28.1	18.6	9.9	11.8	17.3	26.1	44.0
StarMap [†]		89.4	71.1	47.2	22.9	59.5	34.4	13.9	3.7	9.0	17.6	34.1	63.0
NeMo [†]	✓	84.1	73.1	59.9	41.3	60.4	45.1	30.2	14.5	9.3	15.6	24.1	41.8
NeMo-M [†]	✓	86.7	77.2	65.2	47.1	63.2	49.9	34.5	17.8	8.2	13.0	20.2	36.1
NeMo-S [†]	✓	86.1	76.0	63.9	46.8	61.0	46.3	32.0	17.1	8.8	13.6	20.2	36.5
PoseCon		90.8	76.2	59.3	39.7	67.2	46.4	28.1	12.7	7.1	12.6	23.1	45.5
Ours	✓	92.3	85.7	72.7	49.8	72.2	56.7	38.9	17.9	6.6	9.7	16.0	37.9

Table 1: Evaluation against the state-of-the-art on PASCAL3D (L0) and OccludedPASCAL3D (L1-L3). The results are averaged across the 12 object categories and the symbol [†] denotes results taken from [10].

we trained with occlusions produced from PASCAL VOC 2012, and not from MS-COCO [20] as in OccludedPASCAL3D. At the same time, we intentionally use smaller occluders compared to the L1-L3 sets as can be observed by comparing Figure 3 from this text and Figure 1 from the supplementary material.

We evaluate our approach on PASCAL3D [66], its synthetically occluded counterpart OccludedPASCAL3D [10], and KITTI3D [8]. Unless stated otherwise, all experiments use surface normal maps. Similar to [10] we assume known center and distance for all samples, however, we train to achieve robustness to bounding box perturbations and avoid over-reliance on 2D detection accuracy by employing training time bounding box augmentations. We further increase the training data variance through horizontal flipping, color jittering, gaussian blurring, bounding box perturbations, and synthetic occlusions.

We compare the performance of our approach against a category-agnostic classifier Res50-A and a category-specific classifier Res50-S from [10] as well as three state-of-the-art competing methods, namely StarMap [43], NeMo [10], and PoseContrast [58]. For NeMo, in particular, we compare against all three variations termed as NeMo, NeMo-MultiCuboid (NeMo-M), and NeMo-SingleCuboid (NeMo-S). We follow the exact same preprocessing and evaluation methodology as in NeMo and thus borrow their results and the results for Res50-A, Res50-S, and StarMap. PoseContrast, however, was originally trained with more data, so we had to retrain it with the same amount of data as the rest of the methods to ensure a fair comparison. Similar to StarMap and NeMo, we perform the evaluation using three metrics, namely pose accuracy with a threshold of 10° ($ACC_{\frac{\pi}{18}}$) and 30° ($ACC_{\frac{\pi}{6}}$), as well as *Median Error*. Furthermore, we evaluate the inference speed of our approach and compare it against the best competing methods, namely NeMo and PoseContrast.

4.2 Robust and Efficient 3D Pose Estimation

In Tables 1 and 2 we present our performance against the competing methods from [10, 58, 43]. The results in Table 1 are averaged over all object categories for the levels of synthetic occlusion 0% (L0), 20-40% (L1), 40-60% (L2), and 60-80% (L3), respectively. Similar to [10], we use a weighted average that takes into account the number of samples per object category. Overall, our approach outperforms the competing methods across all occlusion levels showcasing the benefit of data augmentation over complex and specialized architectures.

Occl.	Method	aero	bike	boat	bottle	bus	car	chair	table	mbike	sofa	train	tv	Mean
L0	NeMo-M	76.9	82.2	66.5	87.1	93.0	98.0	90.1	80.5	81.8	96.0	89.3	87.1	86.7
	PoseCon.	83.7	84.0	82.5	88.9	97.7	96.7	95.3	86.9	87.2	97.1	96.7	87.8	90.8
	Ours	84.4	88.1	82.5	91.7	98.7	99.2	95.9	88.8	85.6	97.0	98.0	90.0	92.3
L1	NeMo-M	58.1	68.8	53.4	78.8	86.9	94.0	76.0	70.0	61.8	87.3	82.8	82.8	77.2
	PoseCon.	57.7	66.6	56.9	86.7	87.1	83.6	66.9	74.2	72.3	90.6	89.4	78.2	76.2
	Ours	71.4	79.2	70.6	85.2	87.7	97.4	87.2	81.9	78.4	94.1	96.5	80.0	85.7
L2	NeMo-M	43.1	55.7	43.3	69.1	79.8	84.5	58.8	58.4	43.9	76.4	64.3	70.3	65.2
	PoseCon.	38.5	51.2	39.2	81.8	69.5	61.8	49.3	57.6	56.1	74.1	82.4	61.0	59.3
	Ours	54.6	54.6	55.4	68.8	71.0	91.5	66.5	67.8	57.9	84.4	93.1	67.3	72.7
L3	NeMo-M	23.8	34.3	29.5	53.9	56.0	65.5	43.4	41.5	25.4	58.2	43.2	54.1	47.1
	PoseCon.	19.2	30.6	27.4	73.5	47	35.2	33.3	38.0	33.3	52.1	70.7	44.4	39.7
	Ours	27.4	28.8	31.8	43.3	41.3	69.6	40.9	45.6	32.1	62.1	85.2	47.8	49.8

Table 2: $ACC_{\frac{\pi}{6}}$ per PASCAL3D category against the two best competing methods [11, 18].

	$ACC_{\frac{\pi}{6}} \uparrow$				$ACC_{\frac{\pi}{18}} \uparrow$				$MedErr \downarrow$			
	FV	PO	LO	All	FV	PO	LO	All	FV	PO	LO	All
NeMo-S	88.1	72.4	34.9	67.9	70.3	40.4	7.5	43.7	7.3	11.6	46.1	20.0
PoseContrast	97.8	88.5	48.6	80.6	81.6	62.4	18.6	57.5	6.6	8.6	33.0	15.0
Ours	98.1	90.0	56.1	83.4	92.8	70.6	21.0	65.3	3.2	5.4	24.8	10.2

Table 3: Evaluation on cars of KITTI3D without retraining or fine-tuning.

In Table 3, we present our results on KITTI3D. Since the test set of KITTI3D does not provide labels, we split the training set based on the 50-50 split proposed by [11]. NeMo-MultiCuboid requires car type labels and StarMap requires object keypoints which are not provided by KITTI3D, so we evaluate solely against NeMo-SingleCuboid and PoseContrast. Even without retraining or fine-tuning on KITTI3D, our approach exhibits similar performance as in PASCAL3D, outperforming the competing methods in the Fully-Visible (FV), Partly-Occluded (PO) and Largely-Occluded (LO) evaluation categories. At the same time, we demonstrate robustness to out-of-distribution occlusions considering that we trained on cars without same-category occlusions.

To evaluate the effect of occlusion augmentation in our approach, we trained five models with different occlusion scales s_{occ} and evaluated them on L0-L3. As shown in Figure 5, the higher the occlusion scale s_{occ} during training, the more robust the model becomes to higher levels of occlusions. We also note that even on L0 the models trained with synthetic occlusions outperform the ones without demonstrating robustness to real occlusions and clutter.

To evaluate the effect of bounding box augmentation we train five models with different levels of bounding box noise and evaluate each one on increasing levels of test time augmentation. Based on the graphs in Figure 6, training with bounding box augmentations leads to increased robustness to higher β_{test} noise values. However, performance drops slightly for larger β_{train} values when evaluating on the unperturbed datasets ($\beta_{test} = 0$).

To evaluate the inference speed of our approach we count the duration of embedding a query image and retrieving the closest neighbour. We ran this experiment on a consumer-grade GPU, namely NVidia GTX 1050, and averaged the measurements over one thousand runs. Our approach runs at 35fps or requires approximately 29ms per object instance, significantly faster than the 8-second inference of NeMo, but still longer than the 15ms inference

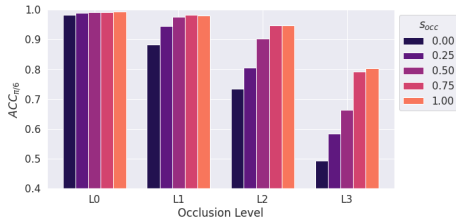


Figure 5: Comparison of models trained with different levels s_{occ} of synthetic occlusion and evaluated on L0-L3.

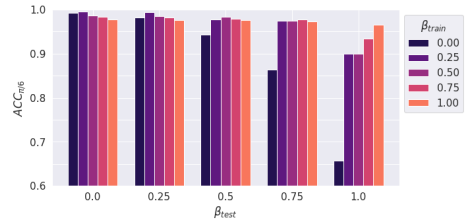


Figure 6: Comparison of models trained with different bounding box noise levels β_{train} on perturbed L0 by β_{test} .

	$ACC_{\frac{\pi}{6}} \uparrow$				$ACC_{\frac{\pi}{18}} \uparrow$				$MedErr \downarrow$			
	L0	L1	L2	L3	L0	L1	L2	L3	L0	L1	L2	L3
Ours	99.2	97.4	91.5	69.6	95.9	89.3	68.8	32.6	3.1	4.2	6.7	16.1
w/o multi-CAD	99.0	97.3	91.8	70.1	96.2	88.1	65.4	30.2	3.0	4.3	7.3	16.2
w/o data augment.	99.2	97.2	90.3	70.7	94.9	85.0	62.9	29.9	3.5	4.7	7.8	16.2
w/ same cat. occl.	99.0	97.1	90.8	68.2	95.8	87.4	64.5	28.6	3.6	4.7	7.5	17.3
w/o contin. labels	98.6	95.5	86.4	59.7	90.4	78.0	54.0	23.0	5.2	6.3	9.3	22.3
w/ Triplet Loss [14]	98.3	94.8	84.6	60.6	93.6	83.6	62.5	31.6	4.2	5.3	7.7	17.1
w/o syn. occlusions	97.8	88.3	74.9	54.6	94.7	67.8	37.7	13.8	3.2	6.9	13.3	25.9
w/o dyn. margin	36.9	36.5	35.8	33.4	25.5	19.2	13.7	7.4	57.9	56.7	53.7	50.0

Table 4: Ablation study results on cars of PASCAL3D L0-L3

time of PoseContrast that uses a mix of classification and regression.

In Figure 7a, we present examples of queries with their corresponding rendered retrievals demonstrating pose estimation accuracy and feature extraction invariant to specific CAD models. In Figure 7b we present failure cases of queries with wrong retrievals which have an angle error higher than 30° . We observe that most failure cases are due to confusion between opposite directions, same-category occlusions, rarely-seen poses, or atypical vehicles. More examples are included in the supplementary material.

4.3 Ablation Study

We conducted an ablation study in which we evaluated our approach for seven distinct cases, as presented in Table 4. First, we trained with only a single CAD model arbitrarily chosen as the sedan for the car category. Second, we trained without appearance augmentations (color jitter, gaussian blur, horizontal flipping). Third, we evaluated our approach with same-category occlusions. Fourth, we used discretized pose labels. Fifth, we used a Triplet loss with a dynamic margin rather than our proposed contrastive loss. Sixth, we trained without synthetic occlusions and in the final case, we removed the dynamic margin. In all cases we observed a non-negligible decrease in performance.

5 Conclusion

Object Pose estimation in a monocular setting is a non-trivial task, especially when dealing with occlusions, clutter, and appearance variations that make handcrafted approaches more

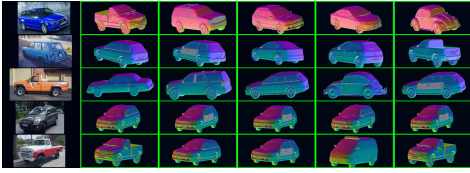
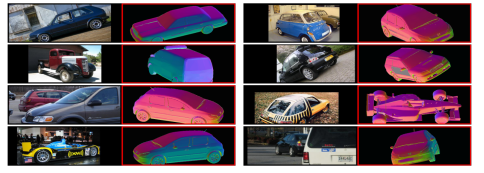
(a) Successful retrievals ($\Delta\theta < 10^\circ$).(b) Failed retrievals ($\Delta\theta > 30^\circ$).

Figure 7: Examples of nearest neighbour retrievals.

prone to error or lack of accuracy. Therefore, we propose learning a pose alignment metric using a contrastive loss with a dynamic margin for comparing object images and renderings with regard to their pose. We reinforce the robustness of the metric using synthetic occlusions and other appearance augmentations. The metric learnt with our Contrastive Pose Loss can be used for pose estimation in an efficient real-time image retrieval setting and achieves state-of-the-art performance on PASCAL3D and OccludedPASCAL3D, as well as high cross-dataset performance on KITTI3D. Finally, our data augmentation scheme can be easily incorporated into other methods to increase their performance.

References

- [1] Wang Angtian, Adam Kortylewski, and Alan Yuille. Nemo: Neural mesh models of contrastive features for robust 3d pose estimation. In *Proceedings International Conference on Learning Representations (ICLR)*, 2021.
- [2] Deniz Beker, Hiroharu Kato, Mihai Adrian Morariu, Takahiro Ando, Toru Matsuoaka, Wadim Kehl, and Adrien Gaidon. Monocular differentiable rendering for self-supervised 3d object detection. In Andrea Vedaldi, Horst Bischof, Thomas Brox, and Jan-Michael Frahm, editors, *Computer Vision – ECCV 2020*, Cham, 2020. Springer International Publishing. ISBN 978-3-030-58589-1.
- [3] Xiaozhi Chen, Kaustav Kundu, Yukun Zhu, Andrew G Berneshawi, Huimin Ma, Sanja Fidler, and Raquel Urtasun. 3d object proposals for accurate object class detection. In C. Cortes, N. Lawrence, D. Lee, M. Sugiyama, and R. Garnett, editors, *Advances in Neural Information Processing Systems*, volume 28. Curran Associates, Inc., 2015. URL <https://proceedings.neurips.cc/paper/2015/file/6da37dd3139aa4d9aa55b8d237ec5d4a-Paper.pdf>.
- [4] Yilun Chen, Shu Liu, Xiaoyong Shen, and Jiaya Jia. Dsgn: Deep stereo geometry network for 3d object detection. In *2020 IEEE/CVF Conference on Computer Vision and Pattern Recognition (CVPR)*, pages 12533–12542, 2020. doi: 10.1109/CVPR42600.2020.01255.
- [5] S. Chopra, R. Hadsell, and Y. LeCun. Learning a similarity metric discriminatively, with application to face verification. In *2005 IEEE Computer Society Conference on Computer Vision and Pattern Recognition (CVPR’05)*, volume 1, pages 539–546 vol. 1, 2005. doi: 10.1109/CVPR.2005.202.
- [6] M. Everingham, L. Van Gool, C. K. I. Williams, J. Winn, and A. Zisserman. The PASCAL Visual Object Classes Challenge 2012 (VOC2012) Re-

- sults, 2012. URL <http://www.pascal-network.org/challenges/VOC/voc2012/workshop/index.html>.
- [7] Divyansh Garg, Yan Wang, Bharath Hariharan, Mark Campbell, Kilian Q. Weinberger, and Wei-Lun Chao. Wasserstein distances for stereo disparity estimation. In *Proceedings of the 34th International Conference on Neural Information Processing Systems*, NIPS’20, Red Hook, NY, USA, 2020. Curran Associates Inc. ISBN 9781713829546.
- [8] Andreas Geiger, Philip Lenz, and Raquel Urtasun. Are we ready for autonomous driving? the kitti vision benchmark suite. In *2012 IEEE Conference on Computer Vision and Pattern Recognition*, pages 3354–3361, 2012. doi: 10.1109/CVPR.2012.6248074.
- [9] Alexander Grabner, Yaming Wang, Peizhao Zhang, Peihong Guo, Tong Xiao, Peter Vajda, Peter M. Roth, and Vincent Lepetit. Geometric correspondence fields: Learned differentiable rendering for 3d pose refinement in the wild. In Andrea Vedaldi, Horst Bischof, Thomas Brox, and Jan-Michael Frahm, editors, *Computer Vision – ECCV 2020*, pages 102–119, Cham, 2020. Springer International Publishing. ISBN 978-3-030-58517-4.
- [10] B. Harwood, V. Kumar B.G., G. Carneiro, I. Reid, and T. Drummond. Smart mining for deep metric learning. In *2017 IEEE International Conference on Computer Vision (ICCV)*, pages 2840–2848, Los Alamitos, CA, USA, oct 2017. IEEE Computer Society. doi: 10.1109/ICCV.2017.307. URL <https://doi.ieeecomputersociety.org/10.1109/ICCV.2017.307>.
- [11] Kaiming He, Xiangyu Zhang, Shaoqing Ren, and Jian Sun. Deep residual learning for image recognition. In *2016 IEEE Conference on Computer Vision and Pattern Recognition (CVPR)*, pages 770–778, 2016. doi: 10.1109/CVPR.2016.90.
- [12] Tong He and Stefano Soatto. Mono3d++: Monocular 3d vehicle detection with two-scale 3d hypotheses and task priors. *Proceedings of the AAAI Conference on Artificial Intelligence*, 33:8409–8416, 07 2019. doi: 10.1609/aaai.v33i01.33018409.
- [13] Alexander Hermans, Lucas Beyer, and Bastian Leibe. In defense of the triplet loss for person re-identification. *CoRR*, abs/1703.07737, 2017. URL <http://arxiv.org/abs/1703.07737>.
- [14] Shun Iwase, Xingyu Liu, Rawal Khirodkar, Rio Yokota, and Kris M. Kitani. Re-pose: Fast 6d object pose refinement via deep texture rendering. In *Proceedings of the IEEE/CVF International Conference on Computer Vision (ICCV)*, pages 3303–3312, October 2021.
- [15] Justin Johnson, Nikhila Ravi, Jeremy Reizenstein, David Novotny, Shubham Tulsiani, Christoph Lassner, and Steve Branson. Accelerating 3d deep learning with pytorch3d. In *SIGGRAPH Asia 2020 Courses*, SA ’20, New York, NY, USA, 2020. Association for Computing Machinery. ISBN 9781450381123. doi: 10.1145/3415263.3419160. URL <https://doi.org/10.1145/3415263.3419160>.
- [16] Diederik P. Kingma and Jimmy Ba. Adam: A method for stochastic optimization. In Yoshua Bengio and Yann LeCun, editors, *3rd International Conference on Learning Representations, ICLR 2015, San Diego, CA, USA, May 7-9, 2015, Conference Track Proceedings*, 2015. URL <http://arxiv.org/abs/1412.6980>.

- [17] Huifang Kong, Tiankuo Liu, Jie Hu, Yao Fang, and Jixing Sun. Unsupervised monocular depth and pose estimation using multiple masks based on photometric and geometric consistency. In *2020 Chinese Automation Congress (CAC)*, pages 3558–3563, 2020. doi: 10.1109/CAC51589.2020.9326951.
- [18] Peiliang Li, Xiaozhi Chen, and Shaojie Shen. Stereo r-cnn based 3d object detection for autonomous driving. In *2019 IEEE/CVF Conference on Computer Vision and Pattern Recognition (CVPR)*, pages 7636–7644, 2019. doi: 10.1109/CVPR.2019.00783.
- [19] Kyaw Zaw Lin, Weipeng Xu, Qianru Sun, Christian Theobalt, and Tat-Seng Chua. Learning a disentangled embedding for monocular 3d shape retrieval and pose estimation. *CoRR*, abs/1812.09899, 2018. URL <http://arxiv.org/abs/1812.09899>.
- [20] T. Lin, P. Goyal, R. Girshick, K. He, and P. Dollar. Focal loss for dense object detection. *IEEE Transactions on Pattern Analysis & Machine Intelligence*, 42(02):318–327, feb 2020. ISSN 1939-3539. doi: 10.1109/TPAMI.2018.2858826.
- [21] Tsung-Yi Lin, Michael Maire, Serge Belongie, James Hays, Pietro Perona, Deva Ramanan, Piotr Dollár, and C. Lawrence Zitnick. Microsoft coco: Common objects in context. In David Fleet, Tomas Pajdla, Bernt Schiele, and Tinne Tuytelaars, editors, *Computer Vision – ECCV 2014*, pages 740–755, Cham, 2014. Springer International Publishing. ISBN 978-3-319-10602-1.
- [22] R. Manmatha, Chao-Yuan Wu, Alexander Smola, and Philipp Krahenbuhl. Sampling matters in deep embedding learning. In *2017 IEEE International Conference on Computer Vision (ICCV)*, pages 2859–2867, 10 2017. doi: 10.1109/ICCV.2017.309.
- [23] Kevin Musgrave, Serge Belongie, and Ser-Nam Lim. Pytorch metric learning, 2020. URL <https://github.com/KevinMusgrave/pytorch-metric-learning>.
- [24] Christos Papaioannidis and Ioannis Pitas. 3d object pose estimation using multi-objective quaternion learning. *IEEE Transactions on Circuits and Systems for Video Technology*, 30(8):2683–2693, 2020. doi: 10.1109/TCSVT.2019.2929600.
- [25] Adam Paszke, Sam Gross, Francisco Massa, Adam Lerer, James Bradbury, Gregory Chanan, Trevor Killeen, Zeming Lin, Natalia Gimelshein, Luca Antiga, Alban Desmaison, Andreas Kopf, Edward Yang, Zachary DeVito, Martin Raison, Alykhan Tejani, Sasank Chilamkurthy, Benoit Steiner, Lu Fang, Junjie Bai, and Soumith Chintala. Pytorch: An imperative style, high-performance deep learning library. In H. Wallach, H. Larochelle, A. Beygelzimer, F. d'Alché-Buc, E. Fox, and R. Garnett, editors, *Advances in Neural Information Processing Systems 32*, pages 8024–8035. Curran Associates, Inc., 2019. URL <http://papers.neurips.cc/paper/9015-pytorch-an-imperative-style-high-performance-deep-learning-library.pdf>.
- [26] Joshua David Robinson, Ching-Yao Chuang, Suvrit Sra, and Stefanie Jegelka. Contrastive learning with hard negative samples. In *International Conference on Learning Representations*, 2021. URL <https://openreview.net/forum?id=CR1XOQ0Uth->.

- [27] Lounès Saadi, Bassem Besbes, Sébastien Kramm, and Abdelaziz Bensrhair. Optimizing rgb-d fusion for accurate 6dof pose estimation. *IEEE Robotics and Automation Letters*, 6(2):2413–2420, 2021. doi: 10.1109/LRA.2021.3061347.
- [28] Florian Schroff, Dmitry Kalenichenko, and James Philbin. Facenet: A unified embedding for face recognition and clustering. *2015 IEEE Conference on Computer Vision and Pattern Recognition (CVPR)*, Jun 2015. doi: 10.1109/cvpr.2015.7298682. URL <http://dx.doi.org/10.1109/CVPR.2015.7298682>.
- [29] Hao Su, Charles R. Qi, Yangyan Li, and Leonidas J. Guibas. Render for cnn: Viewpoint estimation in images using cnns trained with rendered 3d model views. In *2015 IEEE International Conference on Computer Vision (ICCV)*, pages 2686–2694, 2015. doi: 10.1109/ICCV.2015.308.
- [30] I. Sárándi, T. Linder, K. O. Arras, and B. Leibe. How robust is 3d human pose estimation to occlusion? In *IEEE/RSJ Int. Conference on Intelligent Robots and Systems (IROS) Workshops*, 2018.
- [31] Meng Tian, Liang Pan, Marcelo H Ang Jr, and Gim Hee Lee. Robust 6d object pose estimation by learning rgb-d features. In *International Conference on Robotics and Automation (ICRA)*, 2020.
- [32] S. Tulsiani, J. Carreira, and J. Malik. Pose induction for novel object categories. In *2015 IEEE International Conference on Computer Vision (ICCV)*, pages 64–72, Los Alamitos, CA, USA, dec 2015. IEEE Computer Society. doi: 10.1109/ICCV.2015.16. URL <https://doi.ieeecomputersociety.org/10.1109/ICCV.2015.16>.
- [33] Rui Wang, Nan Yang, Jörg Stückler, and Daniel Cremers. Directshape: Direct photometric alignment of shape priors for visual vehicle pose and shape estimation. In *2020 IEEE International Conference on Robotics and Automation (ICRA)*, pages 11067–11073, 2020. doi: 10.1109/ICRA40945.2020.9197095.
- [34] Xun Wang, Xintong Han, Weilin Huang, Dengke Dong, and Matthew R Scott. Multi-similarity loss with general pair weighting for deep metric learning. In *Proceedings of the IEEE Conference on Computer Vision and Pattern Recognition (CVPR)*, pages 5022–5030, 2019.
- [35] Paul Wohlhart and Vincent Lepetit. Learning descriptors for object recognition and 3d pose estimation. In *2015 IEEE Conference on Computer Vision and Pattern Recognition (CVPR)*, pages 3109–3118, 2015. doi: 10.1109/CVPR.2015.7298930.
- [36] Yu Xiang, Roozbeh Mottaghi, and Silvio Savarese. Beyond pascal: A benchmark for 3d object detection in the wild. In *IEEE Winter Conference on Applications of Computer Vision*, pages 75–82, 2014. doi: 10.1109/WACV.2014.6836101.
- [37] Yu Xiang, Tanner Schmidt, Venkatraman Narayanan, and Dieter Fox. Posecnn: A convolutional neural network for 6d object pose estimation in cluttered scenes. *CoRR*, abs/1711.00199, 2017. URL <http://arxiv.org/abs/1711.00199>.
- [38] Y. Xiao, Y. Du, and R. Marlet. Posecontrast: Class-agnostic object viewpoint estimation in the wild with pose-aware contrastive learning. In *2021 International Conference on 3D Vision (3DV)*, pages 74–84, Los Alamitos, CA, USA, dec 2021.

- IEEE Computer Society. doi: 10.1109/3DV53792.2021.00018. URL <https://doi.ieeecomputersociety.org/10.1109/3DV53792.2021.00018>.
- [39] Yang Xiao, Xuchong Qiu, Pierre-Alain Langlois, Mathieu Aubry, and Renaud Marlet. Pose from shape: Deep pose estimation for arbitrary 3D objects. In *British Machine Vision Conference (BMVC)*, 2019.
- [40] Hong Xuan, Abby Stylianou, Xiaotong Liu, and Robert Pless. Hard negative examples are hard, but useful. In Andrea Vedaldi, Horst Bischof, Thomas Brox, and Jan-Michael Frahm, editors, *Computer Vision – ECCV 2020*, pages 126–142, Cham, 2020. Springer International Publishing. ISBN 978-3-030-58568-6.
- [41] Sergey Zakharov, Wadim Kehl, Benjamin Planche, Andreas Hutter, and Slobodan Ilic. 3d object instance recognition and pose estimation using triplet loss with dynamic margin. *2017 IEEE/RSJ International Conference on Intelligent Robots and Systems (IROS)*, Sep 2017. doi: 10.1109/iros.2017.8202207. URL <http://dx.doi.org/10.1109/IROS.2017.8202207>.
- [42] Sergey Zakharov, Ivan S. Shugurov, and Slobodan Ilic. Dpod: 6d pose object detector and refiner. *2019 IEEE/CVF International Conference on Computer Vision (ICCV)*, pages 1941–1950, 2019.
- [43] Xingyi Zhou, Arjun Karapur, Linjie Luo, and Qixing Huang. Starmap for category-agnostic keypoint and viewpoint estimation. *European Conference on Computer Vision (ECCV)*, 2018.

A Supplementary Material

In this supplementary material, we present some additional information about our work to give more insight into the data and performance of our approach. First, we present an overview of the data in PASCAL3D, OccludedPASCAL3D, and KITTI3D. Second, we evaluate the performance of our approach with different rendering types. Third, we present a more detailed view of the experiments on PASCAL3D and OccludedPASCAL3D and how our approach performed on each object category and for each occlusion level. Then we showcase three different reference set designs that were examined and evaluated to determine the optimal choice with regard to performance and inference speed. Afterwards, we provide a more detailed analysis on occlusion and bounding box augmentations, while finally, we include some qualitative results in the form of image retrievals and failure cases.

A.1 Data Overview

In this section we present an overview of the data in PASCAL3D and OccludedPASCAL3D starting with Table 5 that contains the number of samples and number of CAD models per object category and per occlusion category of PASCAL3D and OccludedPASCAL3D. Then we present some example images from all object categories and all occlusion categories in Figure 8, as well as renderings for all CAD models in Figure 9. Furthermore, we include a similar overview of KITTI3D in Table 6 and Figure 10.

Samples	aero	bike	boat	bottle	bus	car	chair	table	mbike	sofa	train	tv	Total	
Train	986	661	1099	745	548	2763	526	1160	624	642	662	629	11068	
Test	L0	969	645	1059	747	532	2712	507	1153	596	624	646	622	10812
	L1	951	634	921	732	527	2646	496	1145	578	542	633	616	10421
	L2	937	619	905	725	525	2612	483	1107	570	521	613	602	10219
	L3	903	601	887	720	521	2573	472	1075	555	507	583	586	9983
CADs	8	6	6	8	6	10	10	6	5	6	4	4	79	

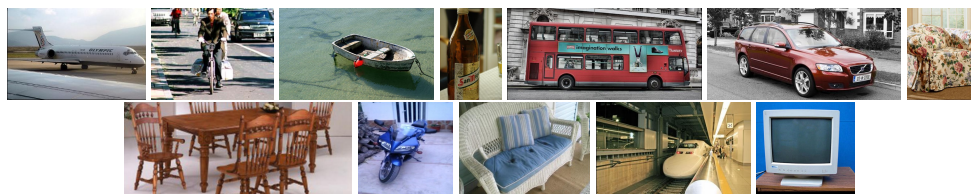
Table 5: Number of samples and number of CAD models per object category of test sets L0-L3 from PASCAL3D and OccludedPASCAL3D

A.2 Evaluation of Rendering Types

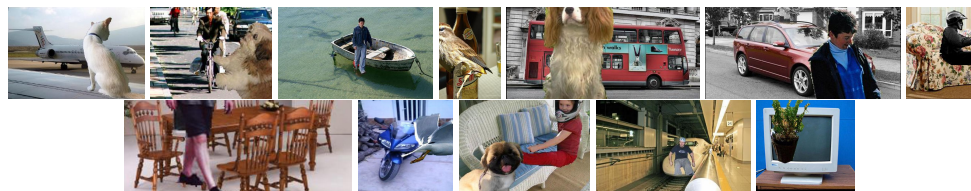
We evaluated five different rendering types, namely, RGB renderings, silhouettes, depth, normals, and triplets (concatenations of RGB, depth, and normals). According to the results in Table 7, we observe that surface normals are more robust to higher levels of occlusions, although, our approach achieves satisfactory performance in all cases. Overall, by observing the standard deviation, all renderings seem to perform similarly in *L0*, but as the difficulty increases towards *L3* the performance varies more widely, making the superiority of surface normal maps more evident.

A.3 Results per Object Category

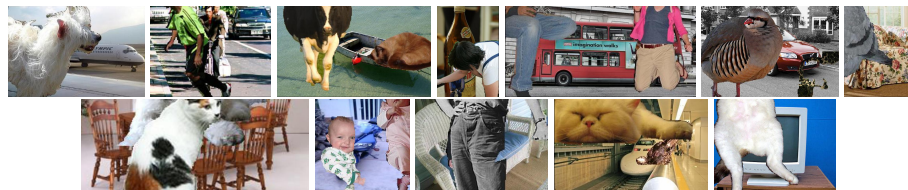
In Tables 8-11, we present the performance of our approach per object category against the competing methods, StarMap and NeMo, on PASCAL3D (*L0*) and OccludedPASCAL3D (*L1-L3*). To compute the average across all object categories we use a weighted average,



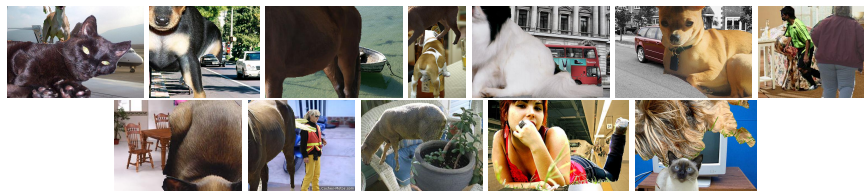
(a) L0



(b) L1



(c) L2



(d) L3

Figure 8: Sample images from the 12 categories of PASCAL3D (L0) and OccludedPASCAL3D (L1-L3) demonstrating the level of occlusion per occlusion category.

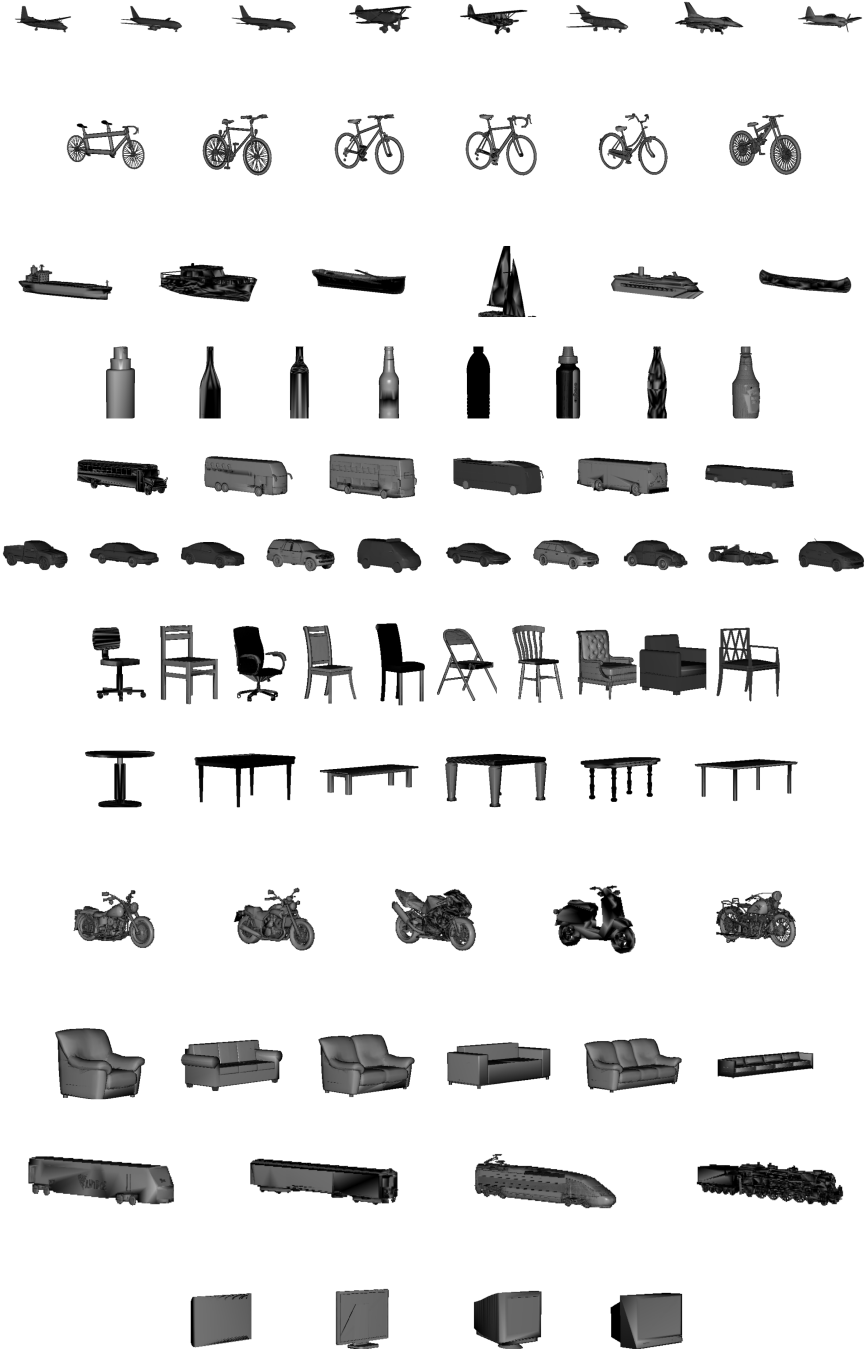


Figure 9: CAD Models per object category of PASCAL3D, from top to bottom, aeroplane, bicycle, boat, bottle, bus, car, chair, diningtable, motorbike, sofa, train, tvmonitor.

Split	Frames	Object Instances by Occlusion Level			
		FullyVis.	PartlyOcc.	MostlyOcc.	Total
Train	3712	3036	1861	1541	6438
Val	3769	2895	1950	2035	6880
Test	7518	-	-	-	-

Table 6: Distribution of KITTI3D car instances (w,h > 40 px)

Rendering	$ACC_{\frac{\pi}{6}} \uparrow$				$ACC_{\frac{\pi}{18}} \uparrow$				$MedErr \downarrow$			
	L0	L1	L2	L3	L0	L1	L2	L3	L0	L1	L2	L3
RGB	99.3	97.7	90.1	67.7	95.9	86.6	64.1	30.4	3.0	4.5	7.5	17.1
Silhouette	99.2	97.1	89.0	62.0	96.3	86.7	65.5	30.0	3.2	4.4	7.1	18.4
Depth	99.1	97.4	90.0	64.9	96.0	87.0	62.2	25.1	3.0	4.4	7.1	18.4
Normals	99.2	97.4	91.5	69.6	95.9	88.3	68.8	32.6	3.1	4.2	6.7	16.1
Triplet	99.2	97.2	90.8	67.9	96.0	86.8	64.3	27.9	3.1	4.3	7.5	18.0

Table 7: Comparison of rendering types on cars of PASCAL3D L0-L3

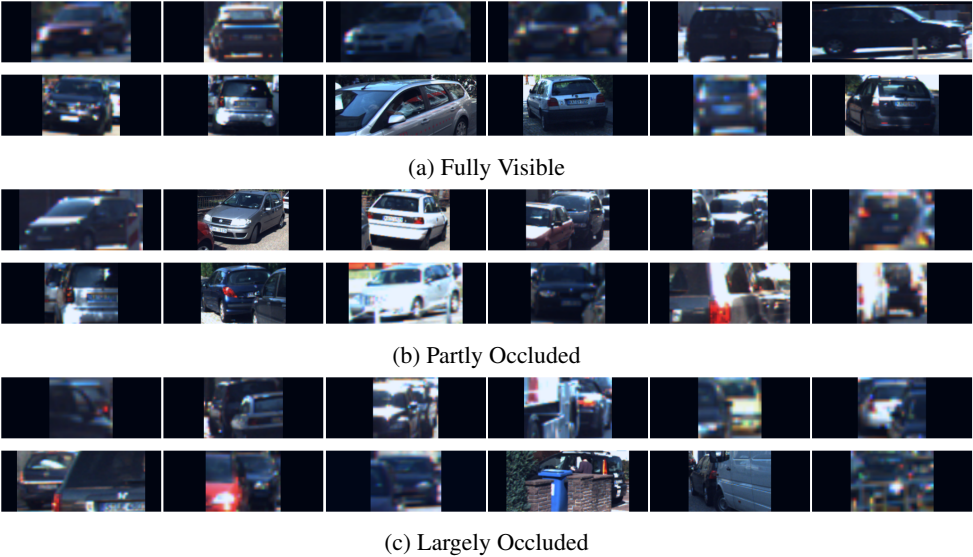


Figure 10: Sample images from KITTI3D demonstrating the level of occlusion per occlusion category.

where the weight of each category is its number of samples divided by the total number of samples, as shown in Table 5. As observed in the aforementioned tables, we outperform the state-of-the-art methods in the vast majority of object categories and occlusion levels. In Table 12, we demonstrate the consistent performance of our approach across five models, trained from scratch on PASCAL3D with surface normal renderings. The standard deviation is less than 3% in all metrics and all five models outperform the state-of-the-art.

		aero	bike	boat	bottle	bus	car	chair	table	mbike	sofa	train	tv	Mean
$ACC_{\frac{\pi}{6}}$	Res50-A	83.0	79.6	73.1	87.9	96.8	95.5	91.1	82.0	80.7	97.0	94.9	83.3	88.1
	Res50-S	79.5	75.8	73.5	90.3	93.5	95.6	89.1	82.4	79.7	96.3	96.0	84.6	87.6
	StarMap	85.5	84.4	65.0	93.0	98.0	97.8	94.4	82.7	85.3	97.5	93.8	89.4	88.1
	NeMo	73.3	66.4	65.5	83.0	87.4	98.8	82.8	81.9	74.6	94.7	87.0	85.5	84.1
	NeMo-M	76.9	82.2	66.5	87.1	93.0	98.0	90.1	80.5	81.8	96.0	89.3	87.1	86.7
	NeMo-S	82.2	78.4	68.1	88.0	91.7	98.2	87.0	76.9	85.0	95.0	83.0	82.2	86.1
	PoseCon.	83.7	84.0	82.5	88.9	97.7	96.7	95.3	86.9	87.2	97.1	96.7	87.8	90.8
	Ours	84.4	88.1	82.5	91.7	98.7	99.2	95.9	88.8	85.6	97.0	98.0	90.0	92.3
$ACC_{\frac{\pi}{18}}$	Res50-A	31.3	25.7	23.9	35.9	67.2	63.5	37.0	40.2	18.9	62.5	51.2	24.9	44.6
	Res50-S	29.1	22.9	25.3	39.0	62.7	62.9	37.5	42.0	19.5	57.5	50.2	25.4	43.9
	StarMap	49.8	34.2	25.4	56.8	90.3	81.9	67.1	57.5	27.7	70.3	69.7	40.0	59.5
	NeMo	39.0	31.3	29.6	38.6	83.1	94.8	46.9	58.1	29.3	61.1	71.1	66.4	60.4
	NeMo-M	43.1	35.3	36.4	48.6	89.7	95.5	49.5	56.5	33.8	68.8	75.9	56.8	63.2
	NeMo-S	49.7	29.5	37.7	49.3	89.3	94.7	49.5	52.9	29.0	58.5	70.1	42.4	61.1
	PoseCon.	53.3	40.0	50.0	56.1	93.2	88.6	67.3	71.7	37.7	64.7	82.5	50.2	67.2
	Ours	59.5	42.8	54.2	68.7	94.5	95.9	70.4	71.8	33.9	69.9	88.7	58.7	72.2
$MedErr$	Res50-A	13.3	15.9	15.6	12.1	8.9	8.8	11.5	11.4	16.6	8.7	9.9	15.8	11.7
	Res50-S	14.2	17.3	15.4	11.7	9.0	8.8	12.0	11.0	17.1	9.2	10.0	14.9	11.8
	StarMap	10.0	14.0	19.7	8.8	3.2	4.2	6.9	8.5	14.5	6.8	6.7	12.1	9.0
	NeMo	13.8	17.5	18.3	12.8	3.4	2.7	10.7	8.2	16.1	8.0	5.6	6.6	9.3
	NeMo-M	11.8	13.4	14.8	10.2	2.6	2.8	10.1	8.8	14.0	7.0	5.0	8.1	8.2
	NeMo-S	10.1	16.3	14.9	10.2	3.2	3.2	10.1	9.3	14.1	8.6	5.4	12.2	8.8
	PoseCon.	9.3	12.0	10.0	8.8	3.1	3.5	7.1	6.0	12.2	7.8	4.8	9.9	7.1
	Ours	8.2	11.6	9.4	7.1	3.0	3.1	6.7	6.3	13.5	6.5	3.9	8.4	6.6

Table 8: Comparison with competing methods on unoccluded PASCAL3D (L0) per category

		aero	bike	boat	bottle	bus	car	chair	table	mbike	sofa	train	tv	Mean
$ACC_{\frac{\pi}{6}}$	Res50-A	57.3	56.8	51.4	78.3	82.5	80.0	62.3	63.1	61.1	84.9	87.8	69.8	70.4
	Res50-S	54.0	59.5	48.9	84.4	86.1	84.4	67.1	64.9	65.9	87.8	92.4	74.5	73.2
	StarMap	52.6	65.3	42.0	81.8	87.9	86.1	64.5	66.5	62.8	76.9	85.2	59.7	71.1
	NeMo	49.0	51.4	52.9	73.5	82.2	94.3	70.2	67.9	53.8	86.7	75.0	79.4	73.1
	NeMo-M	58.1	68.8	53.4	78.8	86.9	94.0	76.0	70.0	61.8	87.3	82.8	82.8	77.2
	NeMo-S	61.9	63.4	52.9	81.3	84.8	92.7	78.4	68.2	68.9	87.1	80.3	76.9	76.0
	PoseCon	57.7	66.6	56.9	86.7	87.1	83.6	66.9	74.2	72.3	90.6	89.4	78.2	76.2
	Ours	71.4	79.2	70.6	85.2	87.7	97.4	87.2	81.9	78.4	94.1	96.5	80.0	85.7
$ACC_{\frac{\pi}{18}}$	Res50-A	11.8	12.5	12.3	26.5	45.0	40.7	14.7	22.3	10.7	24.4	34.9	13.0	25.3
	Res50-S	12.4	10.7	13.8	30.2	46.9	44.8	21.2	24.0	10.4	28.0	40.6	17.9	28.1
	StarMap	15.6	15.1	10.8	36.2	66.6	58.1	26.6	32.0	14.4	23.8	47.4	13.0	34.4
	NeMo	18.5	19.9	19.1	24.0	72.1	82.0	25.8	35.7	12.6	44.3	54.0	49.0	45.1
	NeMo-M	25.4	23.3	22.9	36.7	86.9	84.8	33.1	36.8	20.8	46.5	61.0	46.3	49.9
	NeMo-S	29.3	18.0	24.3	41.5	76.1	80.5	27.2	31.4	19.4	39.9	55.1	32.0	46.3
	PoseCon.	23.4	24.9	27.7	48.8	73.1	67.4	30.8	48.5	21.8	45.2	65.7	29.2	46.4
	Ours	35.1	25.9	34.7	51.8	74.4	88.3	44.4	53.1	23.9	59.0	81.4	29.9	56.7
$MedErr$	Res50-A	25.3	24.5	29.0	14.9	10.6	11.2	22.4	18.1	23.3	15.5	11.7	21.1	17.9
	Res50-S	26.8	23.7	31.0	13.8	10.5	10.6	18.2	16.7	21.8	13.6	10.9	19.3	17.3
	StarMap	27.3	22.1	38.9	12.9	7.0	8.2	19.1	17.2	21.7	16.8	10.6	24.1	17.6
	NeMo	30.8	29.0	27.3	17.6	5.9	5.1	18.6	14.7	27.4	11.3	8.8	10.2	15.6
	NeMo-M	22.6	18.6	25.8	14.1	4.7	4.6	15.1	13.8	21.2	11.0	8.0	11.3	13.0
	NeMo-S	18.9	23.2	26.7	12.6	5.2	5.4	15.6	15.4	20.1	12.1	8.6	15.3	13.6
	PoseCon.	22.0	18.0	21.6	10.2	6.0	6.6	16.8	10.4	18.1	10.9	7.2	16.7	12.6
	Ours	14.3	15.0	15.2	9.7	4.8	4.2	11.3	9.3	17.1	8.5	5.0	14.8	9.7

Table 9: Comparison with competing methods on OccludedPASCAL3D L1 per category

		aero	bike	boat	bottle	bus	car	chair	table	mbike	sofa	train	tv	Mean
$ACC_{\frac{\pi}{6}}$	Res50-A	33.3	40.2	33.6	70.6	69.5	57.0	41.8	47.4	43.3	66.8	80.4	58.1	52.8
	Res50-S	36.3	44.9	36.1	76.1	73.1	65.5	53.2	49.5	45.4	72.7	88.3	65.0	58.4
	StarMap	28.5	38.9	21.3	65.0	61.7	59.3	37.5	44.7	43.2	55.1	56.4	36.2	47.2
	NeMo	38.2	41.2	39.6	58.3	72.6	84.7	50.7	51.1	34.9	70.1	60.0	64.6	59.9
	NeMo-M	43.1	55.7	43.3	69.1	79.8	84.5	58.8	58.4	43.9	76.4	64.3	70.3	65.2
	NeMo-S	43.4	49.6	43.6	76.0	71.2	83.8	61.9	55.9	50.9	78.3	63.1	68.6	63.9
	PoseCon.	38.5	51.2	39.2	81.8	69.5	61.8	49.3	57.6	56.1	74.1	82.4	61.0	59.3
	Ours	54.6	54.6	55.4	68.8	71.0	91.5	66.5	67.8	57.9	84.4	93.1	67.3	72.7
$ACC_{\frac{\pi}{18}}$	Res50-A	6.1	4.5	7.2	20.1	25.9	21.4	9.5	13.2	6.1	14.0	23.0	8.6	14.5
	Res50-S	5.7	6.9	8.0	25.5	33.9	29.1	13.0	11.6	6.8	18.4	32.0	13.8	18.6
	StarMap	3.8	5.8	2.4	19.7	30.5	24.5	7.7	9.6	5.1	9.6	21.5	5.8	13.9
	NeMo	10.7	10.5	11.3	13.9	55.8	60.6	9.3	20.3	6.3	26.1	34.6	32.1	30.2
	NeMo-M	12.8	16.6	16.8	21.9	62.3	64.6	17.2	20.3	12.3	32.4	38.2	32.7	34.5
	NeMo-S	14.9	11.1	15.6	18.2	56.0	62.4	17.4	18.7	10.2	30.5	36.4	22.4	32.0
	PoseCon.	11.3	13.6	17.3	41.1	46.3	38.2	16.4	28.4	12.3	26.7	44.9	17.9	28.1
	Ours	19.0	14.4	22.3	32.1	50.5	68.8	22.2	29.5	13.3	35.7	67.5	17.6	38.9
$MedErr$	Res50-A	49.3	42.5	58.5	17.7	15.9	21.3	35.4	32.0	36.1	20.3	15.2	25.3	30.4
	Res50-S	45.8	33.9	52.8	16.3	12.4	15.1	27.1	30.9	32.4	18.3	12.3	24.1	26.1
	StarMap	55.2	37.1	69.1	20.6	19.0	21.3	39.2	34.0	35.5	27.0	24.8	40.3	34.1
	NeMo	39.8	37.7	44.2	24.8	8.8	7.7	29.7	28.5	47.5	16.9	18.2	17.0	24.1
	NeMo-M	38.5	26.4	38.2	18.8	7.0	7.3	23.0	23.0	36.0	14.0	14.9	16.1	20.2
	NeMo-S	39.9	30.6	38.8	19.5	8.3	7.8	21.3	24.8	29.5	14.2	16.9	18.5	20.9
	PoseCon.	44.8	29.1	43.8	12.0	10.7	14.9	30.3	20.9	25.5	16.7	11.3	24.7	23.1
	Ours	25.7	26.7	24.6	15.2	9.7	6.7	19.9	17.1	23.9	12.9	6.8	22.5	16

Table 10: Comparison with competing methods on OccludedPASCAL3D L2 per category

		aero	bike	boat	bottle	bus	car	chair	table	mbike	sofa	train	tv	Mean
$ACC_{\frac{\pi}{6}}$	Res50-A	18.3	20.8	21.2	62.1	57.0	36.9	31.1	32.2	24.3	56.2	64.5	53.4	37.8
	Res50-S	20.0	33.4	25.5	67.5	57.8	42.0	40.7	33.9	30.3	56.6	82.8	56.5	43.1
	StarMap	7.6	18.5	10.6	46.3	35.1	25.3	22.5	24.6	15.9	26.4	24.0	19.5	22.9
	NeMo	24.0	31.3	27.4	43.3	48.8	62.8	31.8	29.7	18.4	44.2	34.5	51.4	41.3
	NeMo-M	23.8	34.3	29.5	53.9	56.0	65.5	43.4	41.5	25.4	58.2	43.2	54.1	47.1
	NeMo-S	20.6	33.8	27.6	61.7	49.9	61.8	44.7	41.2	35.3	62.9	47.9	50.2	46.8
	PoseCon.	19.2	30.6	27.4	73.5	47	35.2	33.3	38.0	33.3	52.1	70.7	44.4	39.7
	Ours	27.4	28.8	31.8	43.3	41.3	69.6	40.9	45.6	32.1	62.1	85.2	47.8	49.8
$ACC_{\frac{\pi}{18}}$	Res50-A	1.6	2.3	2.9	11.9	14.4	7.6	3.8	5.7	3.1	7.9	12.7	8.9	6.7
	Res50-S	2.0	5.5	4.8	16.7	21.1	13.1	5.9	5.7	4.3	9.9	22.5	6.0	9.9
	StarMap	0.8	1.7	1.1	11.8	8.3	4.8	2.1	2.6	1.6	2.8	5.2	0.7	3.7
	NeMo	4.4	6.2	6.7	6.8	26.5	31.1	3.4	6.7	2.0	9.3	13.0	16.7	14.5
	NeMo-M	5.5	5.2	7.9	10.8	34.2	37.4	7.4	8.2	4.5	15.8	15.1	15.9	17.8
	NeMo-S	4.7	6.7	8.6	11.7	29.2	33.7	11.0	10.7	4.9	17.8	17.2	10.9	17.1
	PoseCon.	4.0	5.3	7.1	26.8	18.4	13.0	9.1	13.0	5.0	15.2	27.4	11.4	12.7
	Ours	6.5	3.3	9.0	16.9	19.2	32.6	7.2	14.1	3.6	15.4	42.2	7.0	17.9
$MedErr$	Res50-A	69.8	70.9	73.2	22.7	24.9	46.7	41.5	44.4	59.8	26.3	21.3	28.4	46.4
	Res50-S	65.8	47.1	75.8	20.9	18.5	46.6	35.9	49.9	56.3	26.4	15.3	26.5	44.0
	StarMap	87.0	67.6	90.2	32.6	51.3	64.0	60.7	53.2	73.4	51.0	52.7	54.7	63.0
	NeMo	65.3	48.4	65.2	34.5	34.9	17.2	44.6	55.7	74.3	33.7	47.6	29.3	41.8
	NeMo-M	69.8	49.6	63.0	28.2	19.4	14.9	35.4	39.9	60.0	23.7	38.1	27.2	36.1
	NeMo-S	74.8	46.1	70.1	24.5	30.2	16.3	35.2	37.5	50.5	21.5	31.7	29.9	36.5
	PoseCon.	66.8	61	64.7	16.6	34.2	51.5	41.4	42.5	50.7	28.7	16.7	33.3	45.5
	Ours	75.2	54.5	61.9	48.8	53.8	16.1	36.8	34.2	49.2	23.8	11.8	31.1	37.9

Table 11: Comparison with competing methods on OccludedPASCAL3D L3 per category

Model	$ACC_{\frac{\pi}{6}} \uparrow$				$ACC_{\frac{\pi}{18}} \uparrow$				$MedErr \downarrow$			
	L0	L1	L2	L3	L0	L1	L2	L3	L0	L1	L2	L3
1	99.2	97.4	91.5	69.6	95.9	89.3	68.8	32.6	3.1	4.2	6.7	16.1
2	99.2	97.0	90.2	69.4	96.2	87.2	66.0	29.7	3.2	4.5	7.2	16.5
3	99.1	97.6	90.3	66.5	95.9	87.7	66.5	30.0	3.2	4.3	7.2	17.4
4	99.2	96.6	90.7	69.9	96.4	88.4	70.2	35.2	3.2	4.1	6.7	14.9
5	99.2	97.4	90.2	69.0	96.0	86.6	63.0	29.3	3.4	4.7	8.0	17.1
Mean	99.2	97.2	90.6	68.9	96.1	87.6	66.7	31.4	3.2	4.4	7.2	16.4
SD	0.04	0.4	0.55	1.37	0.22	0.76	2.84	2.51	0.11	0.24	0.53	0.98

Table 12: Evaluation of performance consistency on PASCAL3D Cars

Set	Azimuth	Elevation	In-plane Rotation	Renderings
TrainDB	-	-	-	2.7k
CoarseDB	5°	5°	5°	178k
FineDB	1°	5°	5°	889k
Range	0°:360°	-30°:60°	-30°:30°	-

Table 13: Discretization of pose space per rendering set

A.4 Evaluation of Reference Set Designs

To decide what is the best reference set design, we trained and evaluated on three distinct reference sets, namely TrainDB, CoarseDB, and FineDB. TrainDB contains the renderings that were generated based on the poses in the training set, while CoarseDB and FineDB were generated using a discretization of the viewing sphere as shown in Table 13. To train more efficiently we sample renderings from CoarseDB and FineDB for every object instance in a batch. To run inference, we examine all possible combinations to find the optimal setting, as presented in Table 14. Out of the three designed reference sets, we found TrainDB to achieve the highest performance thanks to it being more representative of the data while also being the fastest, since it contains the least amount of renderings. Furthermore, we attribute the performance drop of CoarseDB and FineDB to our sampling scheme that does not utilize all the samples, but only the ones close to the training data. Therefore, the models are not trained on all available renderings in the database, so they are not able to project them correctly to the embedding space, thus resulting in the lower performance, seen in Table 14.

A.5 Occlusion Augmentation Results

In Figure 11, we provide graphs of all three evaluation metrics, not just $ACC_{\frac{\pi}{6}}$, for the experiments on our occlusion augmentation scheme. All three metrics follow the same trend indicating that the higher the occlusion scale s_{occ} during training, the higher the robustness across the increasingly occluded sets L0-L3.

A.6 Inference Speed

Our approach can run inference on an object instance in approximately 30ms. Out of those, roughly 60% are spent on embedding the object instance and the rest 40% are spent on calculating the distances and finding the nearest neighbour. Further increasing the inference speed

Training	Inference	fps \uparrow	$ACC_{\frac{\pi}{6}} \uparrow$				$ACC_{\frac{\pi}{18}} \uparrow$				$MedErr \downarrow$			
			L0	L1	L2	L3	L0	L1	L2	L3	L0	L1	L2	L3
TrainDB	TrainDB	35	99.2	97.4	91.5	69.6	95.9	89.3	68.8	32.6	3.1	4.2	6.7	16.1
CoarseDB	TrainDB	35	99.2	97.4	89.1	65.4	95.6	85.2	60.0	25.6	3.2	4.7	8.1	19.9
CoarseDB	CoarseDB	2.5	99.0	95.7	84.5	56.0	91.0	74.0	44.2	14.4	4.2	6.1	11.2	26.2
CoarseDB	Both	0.5	99.0	95.6	84.5	56.0	91.6	74.9	45.2	14.8	3.5	5.8	11.1	26.2
FineDB	TrainDB	35	99.3	96.7	90.9	68.9	95.8	86.6	64.3	30.3	3.2	4.6	7.4	17.4
FineDB	FineDB	0.5	97.6	92.5	81.5	52.0	90.7	75.7	48.0	15.7	4.3	6.2	10.4	28.3
FineDB	Both	0.5	98.0	92.9	82.0	52.3	91.7	76.6	48.9	16.1	3.6	5.8	10.3	28.1

Table 14: Evaluation of the three designed reference sets

can be accomplished by training a smaller backbone (e.g. ResNet18), using an embedding size lower than 512, removing very similar poses from TrainDB, or using renderings of only one CAD model. In case of a larger database, it would also be beneficial to employ a kd-tree to speed up the nearest neighbour search.

A.7 Bounding Box Augmentation Results

In Figure 12, we provide graphs of all three evaluation metrics for the experiments on our bounding box augmentation scheme. The three metrics follow a similar trend which denotes that training with higher bounding box noise results in more robustness to test time noise. However, training with too high β_{train} can result in a performance drop in cases of minimal test time noise, which could be potentially alleviated by training for more epochs. Nevertheless, training with $\beta_{train} \in [0.1, 0.25]$ seems a good trade-off between robustness to noise and accuracy in absence of noise.

A.8 Qualitative Results

In this section, we present some additional qualitative results in the form of image/pose retrievals and failures cases, as shown in Figures 13 and 14 for PASCAL3D, and Figures 15 and 16 for KITTI3D.

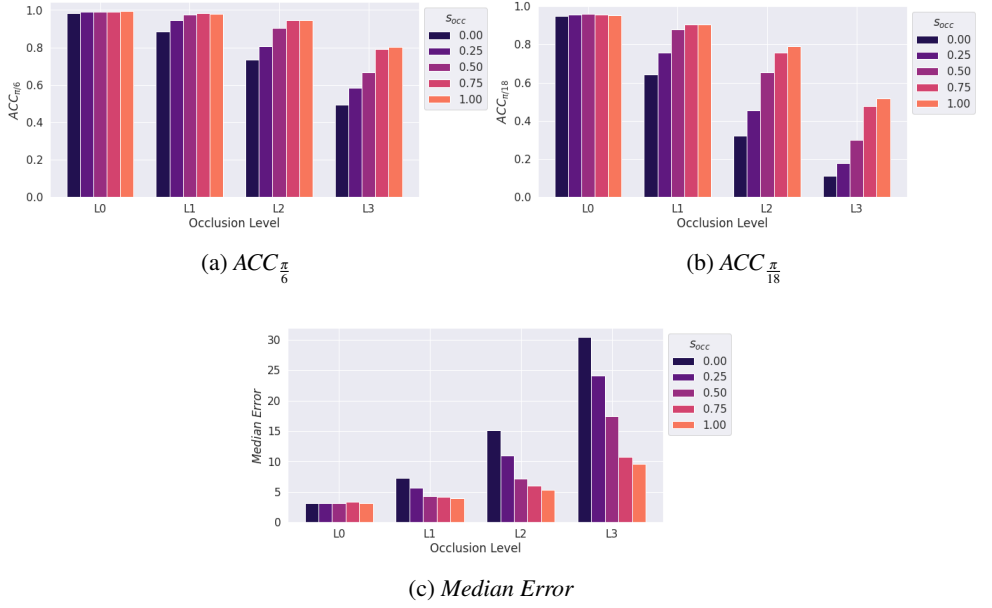


Figure 11: Evaluation of models trained on various occlusion scales s_{occ} on Cars of PASCAL3D and OccludedPASCAL3D.

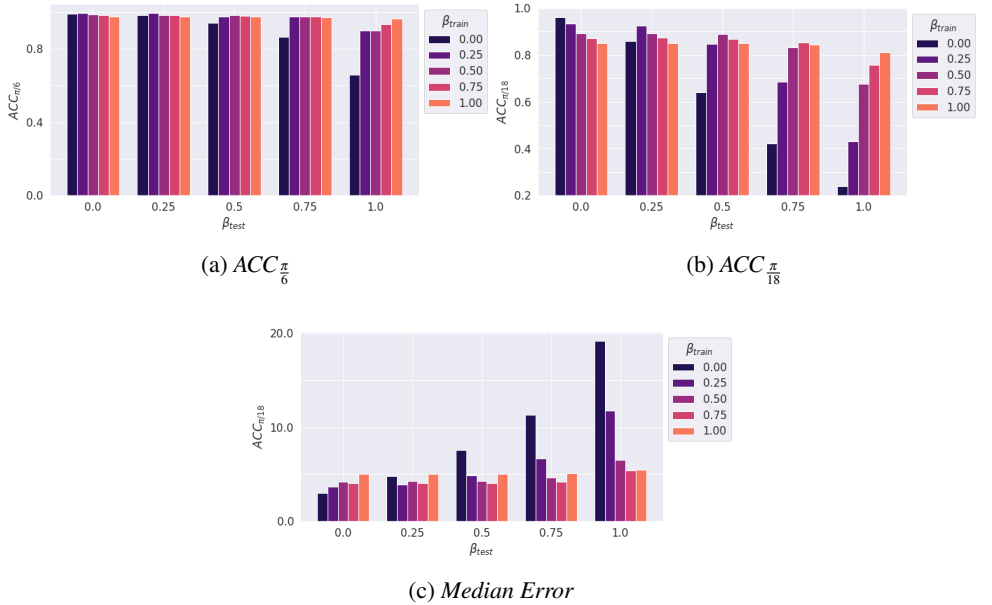
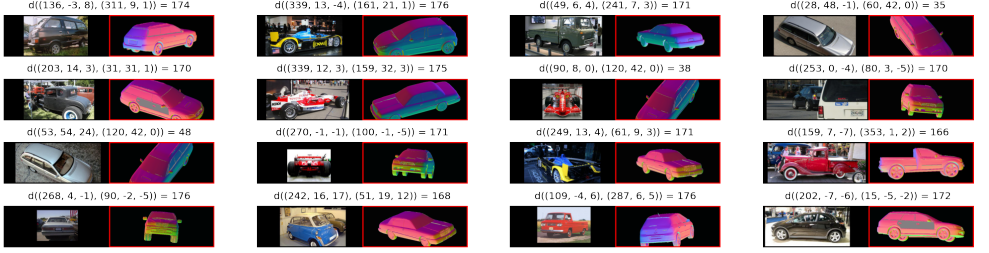


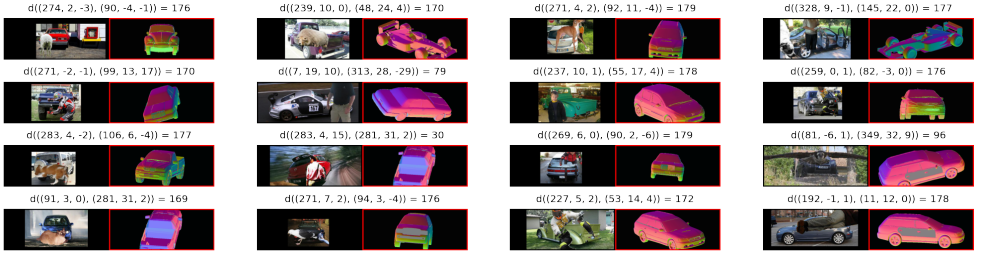
Figure 12: Evaluation of models trained on various levels β_{train} of bounding box augmentation on PASCAL3D L0 Cars with various levels β_{test} of test-time bounding box augmentation.



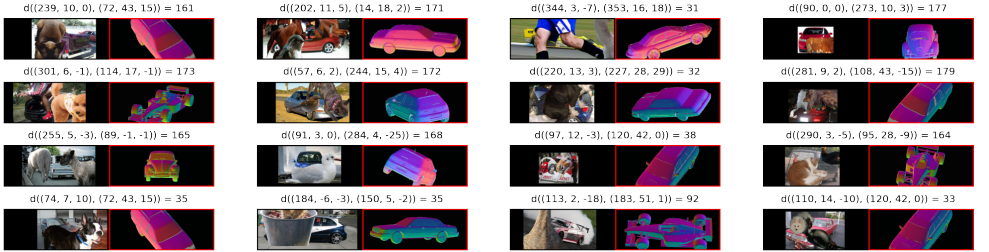
Figure 13: Retrieval of nearest neighbours for occlusion levels L0-L3 in PASCAL3D Cars.



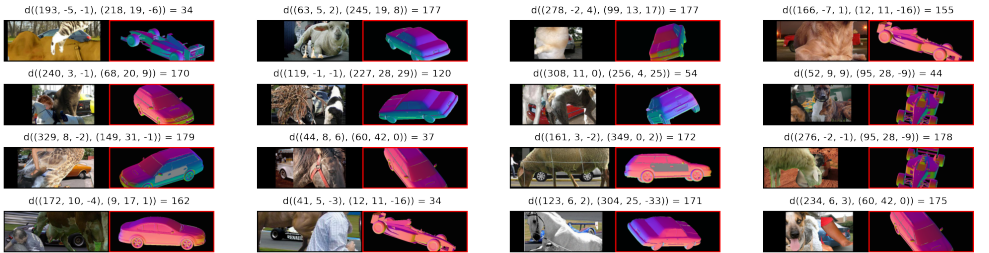
(a) L0



(b) L1



(c) L2

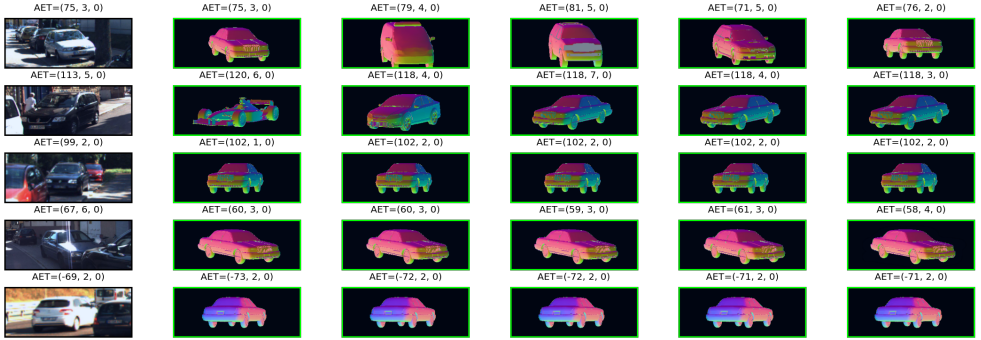


(d) L3

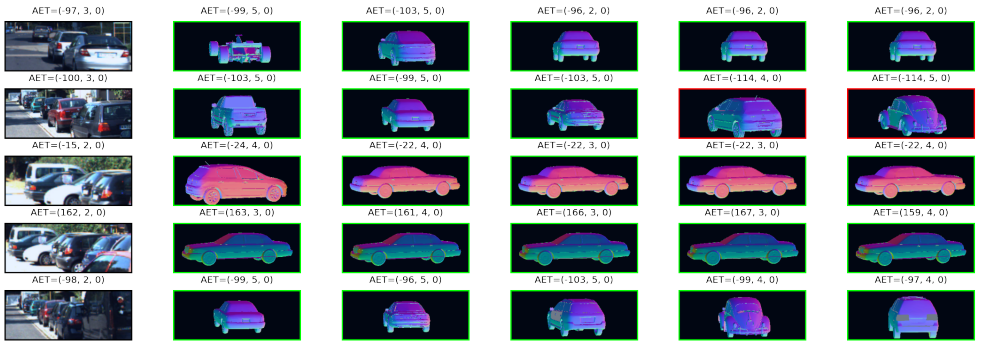
Figure 14: Failure cases for four different levels of occlusion L0-L3 in PASCAL3D Cars.



(a) Fully Visible Objects



(b) Partly Occluded Objects

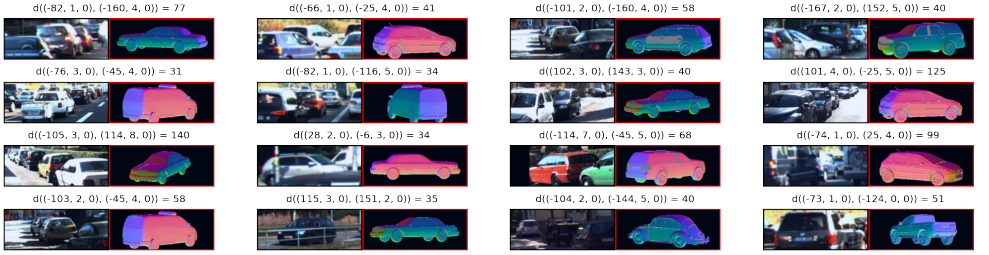


(c) Largely Occluded Objects

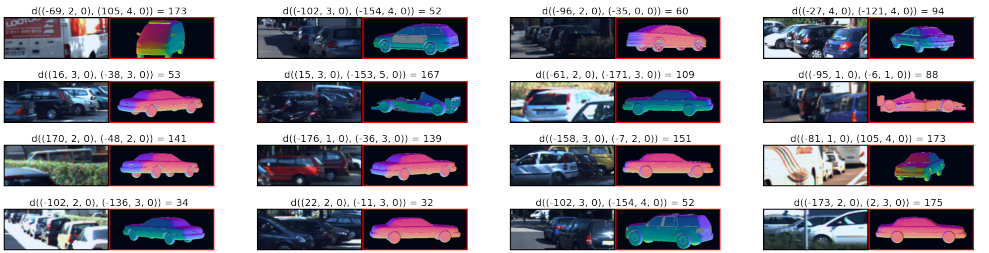
Figure 15: Retrieval of nearest neighbours for three different levels of occlusion in KITTI3D Cars.



(a) Fully Visible



(b) Partly Occluded



(c) Largely Occluded

Figure 16: Failure cases for three different levels of occlusion in KITTI3D Cars.